In Situ High-Pressure Study of Sodium Amide by Raman and Infrared Spectroscopies

Ang Liu and Yang Song*

Department of Chemistry, The University of Western Ontario, London, Ontario N6A 5B7, Canada

Received: August 3, 2010; Revised Manuscript Received: November 10, 2010

Here we report the first in situ high-pressure study of sodium amide ($NaNH_2$) as an agent in potential hydrogen storage applications by using combined Raman and infrared (IR) spectroscopies at room temperature and pressures up to ~16 GPa. Starting with an orthorhombic crystal structure at ambient pressure, sodium amide was found to transform to two new phases upon compression as evidenced by the changes in the characteristic Raman and IR modes as well as by examining the pressure dependences of these modes. Raman and IR measurements on $NaNH_2$ collectively provided consistent information about the structural evolutions of $NaNH_2$ under compression. Upon decompression, all Raman and IR modes were completely recovered, indicating the reversibility of the pressure-induced transformations in the entire pressure region. The combined Raman and IR spectroscopic data together allowed for the analysis of possible structures of the new high-pressure phases of $NaNH_2$.

Introduction

Recently, there has been significant interest in the development of condensed-phase hydrogen storage materials.[1−10] In particular, many studies have focused on lightweight metal hydrides, such as LiH, MgH_2, $LiBH_4$, and $LiNH_2$, due to their outstanding properties for practical applications.[11,12] For instance, lithium amide ($LiNH_2$) with a high gravimetric hydrogen density (18.5 wt %) has exhibited safe, efficient, and reversible hydrogen storage capacities, and thus has been studied extensively.[13−15] Another alkaline amide in the same group, i.e., sodium amide ($NaNH_2$), has also demonstrated promising hydrogen storage capacities. Although $NaNH_2$ has a relatively lower hydrogen content (i.e., 5.2 wt %) than $LiNH_2$, a recent study shows that $NaNH_2$ played an important role in facilitating hydrogen release with other metal hydrides (e.g., $LiAlH_4$) by forming intermediate hydride complexes via ball milling.[16] Compared to $LiNH_2$, however, $NaNH_2$ has as yet not been studied that thoroughly, and as a result, very little is known about its structures or its solid state reactivities in a broad temperature or pressure range that is important for hydrogen storage applications.

As a lightweight metal hydride (density 1.39 g/cm^3), sodium amide crystallizes into an orthorhombic cell under ambient conditions with space group *Fddd* (D_{2h}^{24}) and cell parameters a = 8.964 Å, b = 10.456 Å, c = 8.073 Å, and Z = 16.[17] The unit cell structure of $NaNH_2$ is shown in Figure 1. The sodium and amide ions respectively occupy Wyckoff positions of 16*f* and 16*g*, thus forming a sodium-centered tetrahedral coordination with a Na−N distance of 2.4−2.5 Å. In amide/imide systems, possible hydrogen bonding is typically considered to be an important factor affecting structures and properties of these materials. However, the specific orientation of amide anions and the shortest intermolecular nitrogen−hydrogen distance of 3.56 Å in the unit cell do not seem to facilitate the formation of effective hydrogen bondings. In 1972, Cunningham et al. reported the Raman spectra of solid and molten $NaNH_2$.[18] Isoelectronic with H_2O, NH_2^- ion has a simple C_{2v} symmetry thus giving three fundamental bands, which were subsequently observed and assigned as 3218 cm^{-1} [$\nu_1(A_1)$, symmetric stretch], 1550 cm^{-1} [$\nu_2(A_1)$, bending], and 3267 cm^{-1} [$\nu_3(B_2)$, asymmetric stretch]. The sharp band profile of the fundamental modes of the NH_2^- ions indicated that there is little, if any, hydrogen bonding among NH_2^- ions in either liquid or solid $NaNH_2$, which is consistent with the crystal structure.

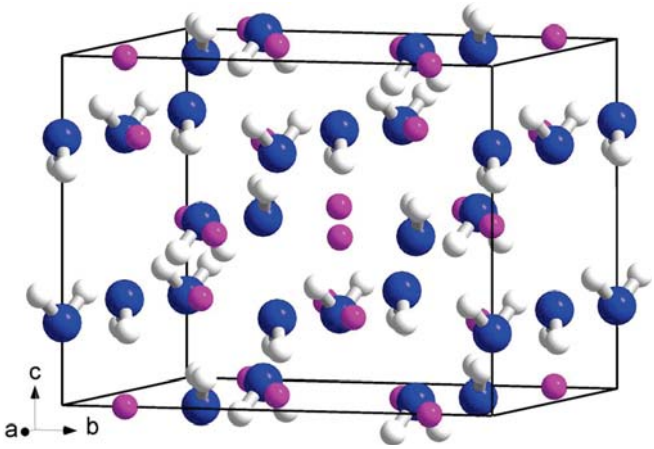

Figure 1. Ambient-pressure crystal structure of $NaNH_2$ in space group *Fddd*. The coordinate system is indicated to show the orientations of the unit cell. The color codes for atoms are pink (sodium), blue (nitrogen), and white (hydrogen).

Since high-pressure technique has demonstrated an effective approach to producing new structures with possibly enhanced hydrogen storage capacities, a wide variety of hydride complexes as potential hydrogen storage materials (e.g., ammonia borane, diborane, calcium borohydride) have been investigated under high pressures.[19−22] In addition, ball milling as a prevailing approach to preparing hydrogen storage materials is a process of driving chemical and structural transformations by external pressure tuning. Therefore, the in-depth investigation of the structures, properties, and transformations of these potential hydrogen storage materials provides an important insight into the understanding of the reaction mechanisms involving hydrogen discharge/recharge and thus the subsequent practical applications in hydrogen storage. Within this context, Chellappa

* To whom correspondence should be addressed. Phone: (519) 661-2111, ext 86310. Fax: (519) 661-3022. E-mail: yang.song@uwo.ca.

10.1021/jp107285r
Published on Web 12/09/2010

et al. recently performed in situ high-pressure Raman spectroscopic studies on $LiNH_2$ up to 25 GPa.[23] In this study, a pressure-induced phase transition was observed to start at 12 GPa and to complete at 14 GPa as characterized by the splitting of the fundamental modes. The new high-pressure phase (labeled as β-$LiNH_2$) was believed to have a crystal structure containing orientational ordering amide anions, different from that of the original α-phase $LiNH_2$. However, the corresponding high-pressure study on $NaNH_2$ has not yet been conducted so far.

In this study, we report the first in situ high-pressure Raman and IR measurements on $NaNH_2$, which was compressed up to 10 and 15 GPa in diamond anvil cells (DACs), respectively. We observed interesting pressure-induced transformations that were in strong contrast to those observed for $LiNH_2$. These findings may help in understanding the different roles of $LiNH_2$ and $NaNH_2$ in their hydrogen storage applications.

Experimental Section

Sodium amide as a fine gray powder with ~95% purity was purchased from Sigma-Aldrich and used without further purification. A symmetrical DAC with two type-I diamonds with 400 μm culets was used for the high-pressure Raman measurements, while a pair of type-II diamonds with a culet size of 600 μm was used for the IR measurements. The sample loading was performed in an MBraun LAB Master 130 glovebox filled with N_2 atmosphere (<10 ppm O_2 and H_2O) and without any fluid pressure transmitting medium to accommodate the hygroscopicity of the material. A few ruby (Cr^{3+}-doped α-Al_2O_3) chips as the pressure calibrant were carefully placed inside the sample chamber before the sample was loaded. The pressure was determined by using the R_1 ruby fluorescence line shift with an accuracy of ±0.05 GPa under quasi-hydrostatic conditions.[24] For the IR measurements, spectral quality KBr powders were also loaded into the DAC used both as pressure transmitting medium and to dilute the sample. In the entire pressure region, ruby fluorescence spectra obtained on different ruby chips across the sample chamber indicated no significant pressure gradient or nonhydrostatic effect.

A customized Raman microspectroscopy system was used to collect the Raman spectra. A 488 nm line from an Innova Ar^+ laser (Coherent Inc.) was used as the excitation source. The laser was focused to <5 μm on the sample by a 20× Mitutoyo objective. The Raman signal was collected with backscattering geometry by using the same objective lens. The Rayleigh scattering was removed by a pair of notch filters that enabled a spectral range of >100 cm^{-1} to be measured. The scattered light was then dispersed using an imaging spectrograph equipped with an 1800 lines/mm grating, achieving a 0.1 cm^{-1} resolution. The Raman signal was recorded using an ultrasensitive, liquid-nitrogen cooled, back-illuminated, charge-coupled device (CCD) detector from Acton. The system was calibrated by neon lines with an uncertainty of ±1 cm^{-1}. To avoid the strong first-order Raman mode of the diamond at 1334 cm^{-1}, the spectra were collected in ranges 100−1300 and 1350−3400 cm^{-1} in several collection windows. For each spectrum, a collection time of 30 s was employed, and the average laser power on the sample was maintained at ~30 mW. All Raman measurements were conducted at room temperature and at pressures of up to ~10 GPa and were reproduced several times.

A customized IR microspectroscopy system was used for all room-temperature IR absorption measurements, and the detailed instrumentations have been described elsewhere.[25] Briefly, a commercial Fourier transform infrared (FTIR) spectrometer from Bruker Optics Inc. (Model Vertex 80v) equipped with a Globar mid-IR light source constituted the main component of the micro-IR system, which was operated under a vacuum of <5 mbar, such that the absorption by H_2O and CO_2 was effectively removed. A collimated IR beam was directed into a relay box through a KBr window on the spectrometer. The beam was then focused onto the sample in the DAC by a 15× reflective objective lens with a numerical aperture of 0.4. The size of the IR beam was set to be identical to the entire sample size (e.g., ~150 μm) by a series of iris apertures. The transmitted IR beam was collected using another identical reflective objective as the condenser, and was directed to a wide-band mercury cadmium telluride (MCT) detector equipped with a ZnSe window that allows measurements in the spectral range 400−10 000 cm^{-1}. All measurements were undertaken in transmission (or absorption) mode. A resolution of 4 cm^{-1} and 512 scans was applied for each spectrum measurement achieving an excellent signal-to-noise ratio. The reference spectrum, i.e., the absorption of diamond anvils loaded with KBr but without any sample, was later divided as background from each sample spectrum to obtain the absorbance.

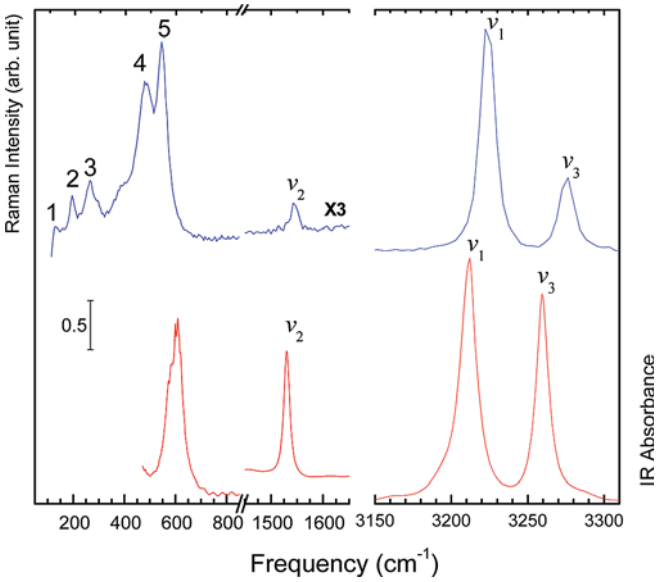

Figure 2. Raman spectrum of $NaNH_2$ (top) in comparison with IR spectrum (bottom) in the spectral region 100−3300 cm^{-1}, both collected at near-ambient pressure and room temperature. The omitted spectral regions are due to the lack of spectroscopic features. The vertical bar labels the scale of the absolute absorbance intensity. The assignment of the vibational modes is labeled above each band.

Results and Discussion

A. Ambient-Pressure Raman and IR Spectra. Raman and IR spectra were collected under ambient conditions as a starting point and are shown in Figure 2. The C_{2v} point group symmetry of NH_2^- predicts that all three vibrational bands ($2A_1 + B_2$) are both Raman and IR active. As expected, three fundamental internal modes were observed at 1536, 3210, and 3261 cm^{-1} in the Raman spectrum, corresponding to the bending mode $\nu_2(A_1)$, the N−H symmetric stretching mode $\nu_1(A_1)$, and the N−H asymmetric stretching mode $\nu_3(B_2)$, respectively. The corresponding IR bands appeared at slightly different frequencies: 1530, 3212, and 3259 cm^{-1}. The sharp Raman modes of the NH_2^- ion are in marked contrast to the Raman spectra of water,[26−28] where the aggregated H_2O molecules linked by hydrogen bonds cause intensive broadening of the fundamentals in both the solid and liquid phases. When compared to the Raman study by Cunningham[18] and the IR study by Nibler et

TABLE 1: Vibrational Frequencies (cm^{-1}) of $NaNH_2$ at Ambient Pressure

		this work		reference				
mode	description	Raman	IR	solid[a]	liquid[a]	IR[b]	Raman[c]	IR[c]
ν_1	symmetric stretch	3210	3212	3218	3218	3212	3258	3258
ν_2	bending	1536	1530	1531	1550	1539	1561	1539
ν_3	asymmetric stretch	3261	3259	3267	3267	3263	3315	3310
5	lattice modes	535	609	522	789		560/550[d]	
4		464		468	506		400[d]	
3		251		349	283			
2		177						
1		115						

[a] Reference 18, Raman measurements. [b] Reference 29. [c] Reference 30, measured for $LiNH_2$. [d] Reference 31, using neutron scattering (see text).

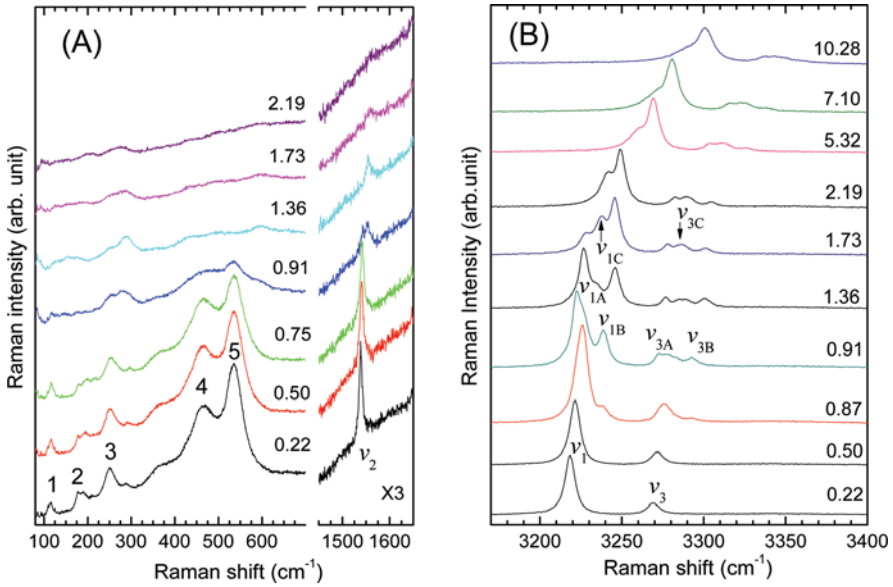

Figure 3. Selected Raman spectra of $NaNH_2$ collected at room temperature on compression in the regions 100−1650 cm^{-1} at pressures of 0.22−2.19 GPa (A) and 3150−3400 cm^{-1} at pressures of 0.22−10.28 GPa (B). The relative intensities are normalized and thus are directly comparable. The pressures in GPa are labeled for each spectrum. The assignments are labeled for selected Raman modes (see text).

al.[29] on the condensed phase of $NaNH_2$, our measurements are in excellent agreement with theirs, as can be seen from Table 1. We also listed the vibrational frequencies of NH_2^- with the other moiety being Li^+ as reported by Bohger et al.[30] All of the frequencies of the internal modes of NH_2^- are higher in $LiNH_2$ than in $NaNH_2$, indicating that the NH_2^- group in $LiNH_2$ is characterized by a shorter N−H distance and thus a higher bond stiffness.

In addition, we also observed five Raman bands at 115, 177, 251, 464, and 535 cm^{-1} which we labeled as 1, 2, 3, 4, and 5, respectively, and one IR band at 609 cm^{-1} in the lattice region. On the basis of the factor group analysis using the established crystal structure of $NaNH_2$, 33 lattice vibrational (21 translational and 12 librational) modes are expected, among which 18 are Raman active and 12 are IR active. Apparently, the observed lattice modes are just a subset of the total predicted modes. The limit of the notch filter used in the Raman measurements and the spectral limit of >400 cm^{-1} imposed by our IR instrument capability may also contribute to the lack of lattice modes observed. Cunningham reported even fewer lattice modes for solid $NaNH_2$ at 522, 468, and 349 cm^{-1}, in rough agreement with our results.[18] Using neutron scattering, Day and Sinclair investigated the vibrational modes of $NaNH_2$ as well.[31] Some strong bands at 560/550 cm^{-1} and a small bump at 400 cm^{-1} were observed in the lattice region, which were attributed to NH_2^- torsion and wagging, respectively. All these comparisons are summarized in Table 1 as well. We therefore tentatively assign Raman lattice modes 1−3 as translational modes and modes 4 and 5 as well as the IR lattice mode as librational modes.

B. Raman Spectra on Compression. Starting from ambient pressure, Raman spectra of $NaNH_2$ were collected upon compression to 10.3 GPa with selected spectra depicted in Figure 3. As can be seen, all the lattice modes were significantly weakened when compressed from ambient pressure to ~0.9 GPa, especially for the librational modes (modes 4 and 5). Above 0.9 GPa, lattice mode 3 was found to split together with the depletion of modes 2 and 4. All these observations strongly suggest a phase transition associated with a significant modification of the crystal structure of $NaNH_2$. Concurrently, the ν_2 H−N−H bending mode exhibited a prominent intensity reduction and apparently developed into a doublet at 0.9 GPa, reinforcing the phase transition evidenced by the lattice modes at this pressure. The most dramatic changes were observed in the ν_1 and ν_3 stretching modes. In particular, the ν_1 mode displayed a shoulder which rapidly developed into a doublet around 0.9 GPa. Further compression resulted in the resolution of a third component together with the weakening of the original component of this mode (e.g., at 1.73 GPa). We labeled these multiple components of this mode with ν_1, ν_{1A}, ν_{1B}, and ν_{1C} in the order of their appearing sequence. Similarly, the ν_3 mode first split into a doublet around 0.9 GPa, which subsequently evolved into a triplet as well (e.g., at 1.73 GPa), and the multiple components were labeled in a way similar to that of the ν_1 mode

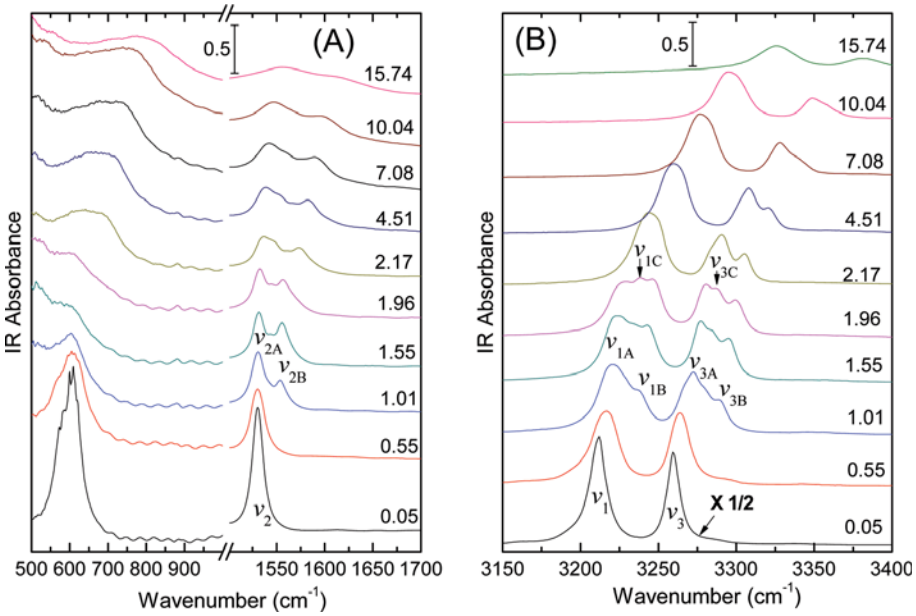

Figure 4. Selected IR spectra of $NaNH_2$ collected at room temperature on compression in the spectral regions 500−1700 cm^{-1} (A) and 3150−3400 cm^{-1} (B) in the pressure region 0.05−15.74 GPa. The vertical bar labels the scale of the absolute absorbance intensity. The pressures in GPa are labeled for each spectrum. The assignments are labeled for selected IR modes (see text).

(Figure 3B). When compressed to ∼2 GPa, another round of changes in the entire spectral region was observed. First of all, no obvious lattice modes were observed above 2 GPa; the ν_2 bending mode was also completely depleted. Furthermore, the obvious characteristic of the stretching modes is the component merging and band broadening. For example, the ν_1 mode displayed a singlet with a front shoulder at 5.3 GPa whereas the ν_3 mode appeared as a single broad band. At the highest pressure of the current study (i.e., 10.3 GPa), all bands became extremely weak and broad with only one dominant peak (i.e., the ν_1 mode) observable.

C. IR Spectra on Compression. Mid-IR spectra of $NaNH_2$ were collected on compression to 15.7 GPa. Selected absorption spectra as a function of pressure in the spectral region 500−3400 cm^{-1} are depicted in Figure 4. Overall, all bands became significantly broadened with increasing pressure. In the lattice region, specifically, the librational mode at ∼600 cm^{-1} first became weakened and broadened when compressed from ambient pressure to ∼1 GPa, followed by the complete depletion at ∼2 GPa, above which pressure an extremely broad IR band was observed in this region all the way to the highest pressure. In contrast, the ν_2 bending mode of the amide anion was found to split into a doublet (labeled as ν_{2A} and ν_{2B}) when compressed to ∼1 GPa. Above 2 GPa, this mode exhibited an abrupt broadening for both components and enhanced separation with progressive compressions. Similar to the Raman measurements, the ν_1 and ν_3 IR modes were also found to split with compression. For example, both modes split into a doublet (labeled as ν_{1A}/ν_{1B} and ν_{3A}/ν_{3B}) which each rapidly evolved into a triplet. Above 2 GPa, the multiple components for both modes started to merge, for example, into a broad singlet for the ν_1 mode and a doublet for the ν_3 mode. When the pressure is sufficiently high, e.g., at ∼7 GPa, both stretching modes display a singlet again as at ambient pressure, except that the bandwidths are much larger.

In summary, these IR spectroscopic observations collectively suggest that the $NaNH_2$ underwent two possible phase transitions at ∼1 and ∼2 GPa, consistent with those identified by Raman measurements. No further dramatic phase transitions were observed up to the highest pressure achieved, indicating that

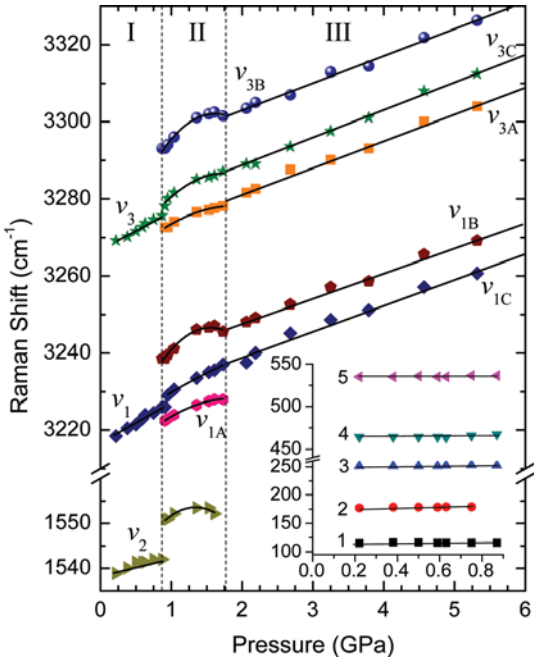

Figure 5. Pressure dependence of Raman modes of $NaNH_2$ on compression. Different symbols represent Raman modes with different origins with assignments labeled (see text). The solid lines crossing the solid symbols are based on linear regressions except for the pressure region of 0.9−2.0 GPa, where quadratic regressions were used for all Raman modes. The vertical dashed lines indicate the proposed phase boundaries.

the third high-pressure phase has a much larger stability region than the previous two.

D. Pressure Effects on Raman and IR Modes. The pressure dependences of the observed Raman and IR internal modes of $NaNH_2$ were examined by plotting the vibrational frequencies as a function of pressure and are shown in Figures 5 and 6. Those for Raman lattice modes are depicted as an inset of Figure 5. The pressure coefficients for these modes are analyzed by a least-squares fitting of the experimental data and are reported in Table 2. In addition to the compelling spectroscopic evidence, possible phase transitions could be further inferred and more

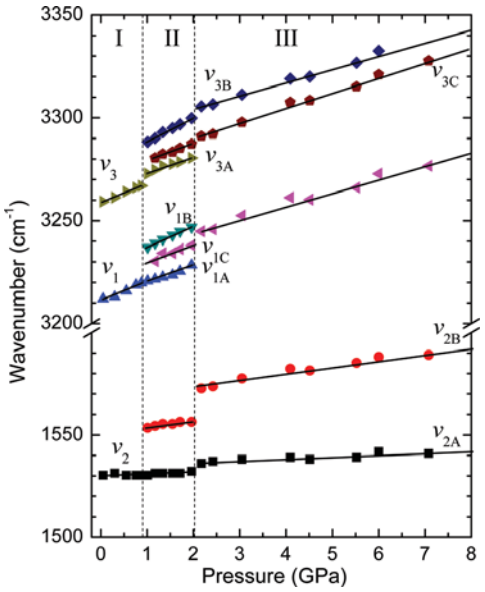

Figure 6. Pressure dependence of IR modes of $NaNH_2$ on compression. Different symbols represent IR modes with different origins with assignments labeled (see text). The solid lines crossing the solid symbols are based on linear regressions. The vertical dashed lines indicate the proposed phase boundaries.

TABLE 2: Pressure Dependence of the Optical Modes of $NaNH_2$ on Compression[a]

optical mode	frequency[b] (cm^{-1})	dν/dP[c] (cm^{-1}·GPa^{-1}) phase I (<0.9 GPa)	phase II[d] (0.9−2.0 GPa)	phase III (>2.0 GPa)
ν_3	3261 (3259)	10.6 (9.6)	11.0 (12.2)	7.0 (6.8)
			9.8 (8.4)	7.4 (7.6)
			6.9 (7.7)	6.8
ν_1	3210 (3212)	11.7 (9.9)	9.5 (10.2)	6.5
			9.9 (8.8)	6.8 (6.6)
			7.1 (7.6)	
ν_2	1536 (1530)	4.9 (0)	1.3 (3.0)	(3.4)
			(1.5)	(1.0)

[a] Values refer to Raman modes while those in parentheses refer to IR modes. [b] Measured at ambient pressure and room temperature. [c] Multiple entries for each mode correspond to the splittings (see Figures 3−6). [d] Quadratic regression was used for Raman modes in this phase, and the values correspond to average dν/dP in this pressure region.

accurately located if sharp changes in the pressure coefficients are observed.

In general, all Raman and IR modes exhibited pressure-induced blue shifts, consistent with the fact that the bonds become stiffened upon compression. In the lattice region, all modes can be fitted using linear functions with slopes of almost zero below 1 GPa, indicating that the interion interactions within the unit cell are not sensitive to compression in this pressure region. In the region for internal vibrational modes, as can be seen, the distinct changes of pressure dependence as well as the appearance/disappearance of the major Raman and IR modes also indicate consistent phase boundaries. In general, the pressure coefficients are largest in the region below 0.9 GPa and decrease progressively across the boundaries around 0.9 and 2.0 GPa. Different pressure dependences are indicative of the different compressiblities of the different phases. We note that linear regressions can be used for all Raman and IR modes in all pressure regions except for the Raman modes in the region 0.9−2 GPa, which can be best fit with quadratic functions. The compression behavior of the Raman modes of $NaNH_2$ in this pressure region is similar to that for $LiNH_2$ in a broad pressure region of 0−14 GPa.[23] Overall, the pressure dependences of the major Raman and IR modes collectively indicate several distinct pressure regions in which $NaNH_2$ could exist in different phases. These pressure regions are <0.9, 0.9−2.0, and >2.0 GPa, which we label as phases I, II, and III, respectively.

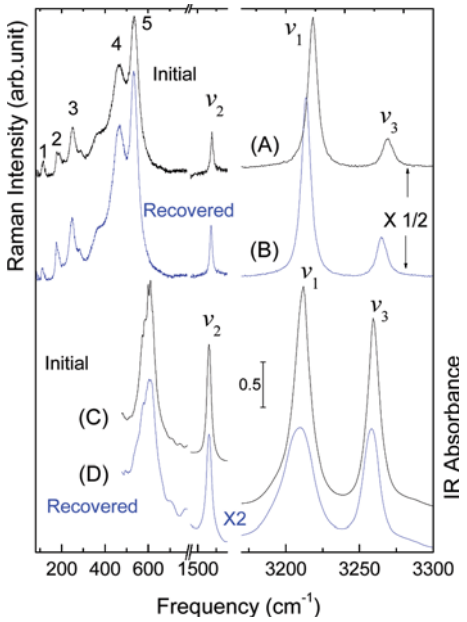

Figure 7. Raman (top) and IR (bottom) spectra of recovered $NaNH_2$ (B and D) upon decompression in comparison with those respective initial near-ambient-pressure spectra before compression (A and C). The Raman intensity is normalized with arbitrary unit labeled along the left vertical axis. The vertical bar indicates the absolute IR absorbance intensity.

E. Raman and IR Spectra on Decompression. Raman and IR spectra were also collected on decompression all the way down to near-ambient pressure in order to better understand the pressure-induced structural evolutions and the high-pressure stability of $NaNH_2$. During decompression, we observed similar back transformations in both Raman and IR spectra with almost identical transformation pressures as in the compression sequence, indicating very minor or almost negligible hysteresis. More importantly, as can be seen in Figure 7, all fundamental modes, including both internal and lattice modes observed before compression (spectra A and C) at ambient pressure were completely recovered upon decompression to near-ambient pressure (spectra B and D). The difference in the Raman shifts before and after compression could be due to the different pressures under which the spectra were collected, whereas the different IR band shapes and intensities could be associated with the modification of the sample thickness in the compression/decompression cycle. All these observations suggest that the pressure-induced structural transformations of $NaNH_2$ are reversible, and that $NaNH_2$ is chemically stable in the entire pressure region used in this study.

F. Discussion. Our Raman and IR measurements collectively and consistently identified two pressure-induced phase transitions. It is therefore of interest to understand the possible structures of the high-pressure phases and thus the nature of the transformations. Phase I (0−0.9 GPa) can be interpreted as the extension of the ambient-pressure orthorhombic crystal structure with the space group $Fddd$ (D_{2h}^{24}) as evidenced by the spectroscopic features in this pressure region. In particular, starting with C_{2v} point group symmetry, the number of vibrational modes and optical activities of NH_2^- can be predicted

TABLE 3: Factor Group Analysis of Vibrational Modes of NH_2^- in Space Group *Fddd* (D_{2h}^{24})

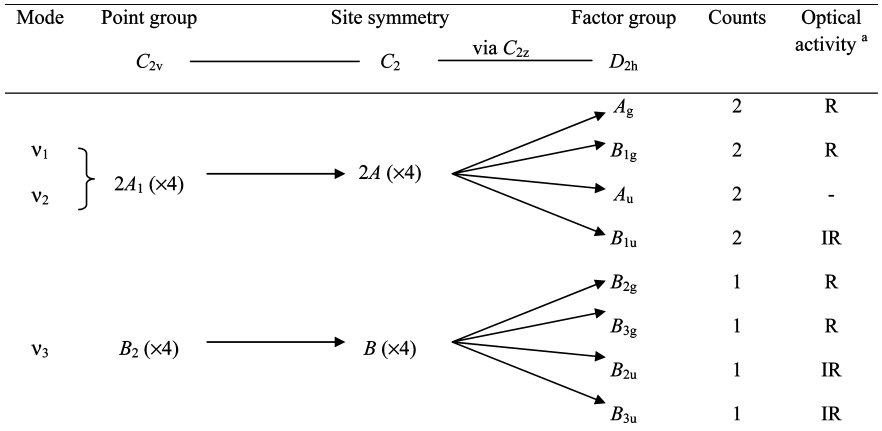

[a] R, Raman active; IR, infrared active.

TABLE 4: Number of Predicted and Observed Fundamental Vibrational Modes of NH_2^- in Different Phases[a]

mode[b]	predicted *Fddd*	observed		
		phase I	phase II	phase III
ν_3 (3269 cm^{-1})	2R + 2IR	1R + 1IR	3R + 3IR	3R + 2IR
ν_1 (3218 cm^{-1})	2R + 1IR	1R + 1IR	3R + 3IR	2R + 1IR
ν_2 (1538 cm^{-1})	2R + 1IR	1R + 1IR	1R + 2IR	2IR

[a] R, Raman active; IR, infrared active. [b] The fundamental vibrational modes are listed in decreasing frequency with Raman shifts measured at ambient pressure labeled.

using factor group analysis as shown in Table 3. By identifying the number of molecules per primitive cell ($Z = 16$ and $Z' = 4$, where Z and Z' are the number of molecules per unit cell and per primitive cell, respectively), the site symmetry from the crystal structure, and the appropriate correlation path, the irreducible representations for the three fundamental frequencies under the *Fddd* factor group are

$$\Gamma(\nu_1 \text{ or } \nu_2) = A_g + B_{1g} + A_u + B_{1u} \quad (1)$$

$$\Gamma(\nu_3) = B_{2g} + B_{3g} + B_{2u} + B_{3u} \quad (2)$$

Therefore, two Raman active modes (A_g and B_{1g}) and one IR active mode (B_{1u}) are expected for each of ν_1 and ν_2, and two Raman (B_{2g} and B_{3g}) and two IR (B_{2u} and B_{3u}) active modes are expected for ν_3. The observation of only one Raman and one IR active mode in the region 0−0.9 GPa suggests that the correlation field splitting is not significant enough to be resolved under the current conditions. These comparisons are summarized in Table 4.

In the pressure region 0.9−2.0 GPa, all of the three fundamental internal modes in both Raman and IR spectra were found to split into a doublet or a triplet as summarized in Table 4, except for the ν_2 mode exhibiting a transient splitting at 0.9 GPa, above which pressure the splitting cannot be obviously identified. These observations suggest that the structure of this phase is characterized by enhanced intermolecular interactions. Since all the internal modes start with a symmetry that is nondegenerate, the static field splitting can therefore be ruled out as the primary cause. Instead, correlation field splitting due to the interaction of nonequivalent molecules within the same unit cell is most likely the mechanism. If there were no major change of the crystal structure of this phase, the doubling of the unit cell content might account for the splitting. However, factor group analysis on the content doubled cell would have predicted doublet and/or quartet bands, rather than triplets as observed. Therefore, it is highly likely that the crystal structure of phase II is significantly different from that in phase I, as also suggested by the Raman lattice features in terms of both the number of modes and the band profiles. To account for the triplet splitting, upon examination of all crystallographic space groups, a possibility is a trigonal or hexagonal group that has a site symmetry with a Wyckoff multiplicity of 3. Of course, the detailed crystal structure of phase II needs to be examined by X-ray diffraction measurements.

Although splittings continued to be observed above 2 GPa, the general trend of band broadening for all modes together with the depleted lattice features in Raman measurements suggests that $NaNH_2$ is transforming into an amorphous phase via a significant structural disordering. This disordering, however, only involves orientation and/or bond length modification of the NH_2^- groups with an intact chemical structure as evidenced by the completely reversible back transformations. Furthermore, the positive pressure shifts of all modes in all pressure regions are consistent with bond stiffening upon compression and are indicative of no hydrogen bonding effect even with significantly shortened intermolecular N···H distances as a result of compression.

We note that although $NaNH_2$ has the identical NH_2^- moiety as $LiNH_2$, their high-pressure behaviors are drastically different. First of all, only one crystalline-to-crystalline phase transition was observed for $LiNH_2$ in the pressure region 12−14 GPa, indicating a much wider phase stability region than phases I and II of $NaNH_2$. The new phase (labeled as β-phase) of $LiNH_2$ has spectroscopic features significantly different from those of the ambient-pressure α-phase (space group $I\bar{4}$) in terms of the much more complicated lattice profile and an N−H stretching mode, indicating a major modification of the crystal and/or molecular structures. Second, the NH_2^- bending mode (ν_2) was not observed/reported for $LiNH_2$. Third, although the pressure-induced phase transitions were found to be reversible for both $NaNH_2$ and $LiNH_2$, the latter exhibited a larger hysteresis during back transformation whereas no hysteresis was observed for $NaNH_2$. Most significantly, $LiNH_2$ remained a perfect crystal even up to 25 GPa with a distinctive orientational ordering of the NH_2^- ions, in strong contrast to the amorphous/disordering behavior of $NaNH_2$ above 2 GPa. In summary, the significantly different compression behavior of $NaNH_2$ from that of $LiNH_2$,

especially in the low-pressure region, may have profound implications in practical applications in that the pressure of a few gigapascals is more readily achievable by ball milling or other approaches. Nonetheless, additional experimental work on $NaNH_2$ and other amides as well as theoretical investigations are still needed to understand this difference and to further explore amide-based hydrogen storage applications.

Conclusions

In situ high-pressure Raman and IR spectroscopic measurements of $NaNH_2$ revealed two pressure-induced phase transitions around 0.9 and 2.0 GPa. These two transitions are evidenced by both the significant changes in spectral profiles and the pressure dependence of Raman and IR modes over different pressure ranges. Upon decompression, all characteristic Raman and IR modes are recovered, indicating that the pressure-induced transitions are completely reversible. Spectral analysis of the combined Raman and IR data indicates that phase I in the pressure region of <0.9 GPa maintains an orthorhombic structure with a space group *Fddd*, the same as that at the ambient-pressure structure. In the pressure region 0.9−2.0 GPa (phase II), the structure of $NaNH_2$ may have a completely different crystal lattice likely with a space group of trigonal or hexagonal symmetry. In the pressure region of >2.0 GPa, the depleted lattice features and broad band profiles in both the Raman and IR measurements suggest that phase III is a disordered or amorphous phase. Further experimental and theoretical investigations may help in better understanding of the structures of the newly discovered high-pressure phases.

Acknowledgment. The authors acknowledge funding support from a Discovery Grant, a Research Tools and Instruments Grant from the Natural Science and Engineering Research Council of Canada, a Leaders Opportunity Fund from the Canadian Foundation for Innovation, an Early Researcher Award from the Ontario Ministry of Research and Innovation, and a Petro-Canada Young Innovator Award from the University of Western Ontario.

References and Notes

(1) Schlapbach, L.; Zuttel, A. *Nature* **2001**, *414*, 353.
(2) Grochala, W.; Edwards, P. P. *Chem. Rev.* **2004**, *104*, 1283.
(3) Vajeeston, P.; Ravindran, P.; Kjekshus, A.; Fjellvag, H. *J. Alloys Compd.* **2005**, *404*, 377.
(4) Goncharov, A. F.; Hemley, R. J. *Chem. Soc. Rev.* **2006**, *35*, 899.
(5) Struzhkin, V. V.; Militzer, B.; Mao, W. L.; Mao, H. K.; Hemley, R. J. *Chem. Rev.* **2007**, *107*, 4133.
(6) Ravindran, P.; Vajeeston, P.; Fjellvag, H.; Kjekshus, A. *Comput. Mater. Sci.* **2004**, *30*, 349.
(7) Kim, J. H.; Jin, S. A.; Shim, J. H.; Cho, Y. W. *Scr. Mater.* **2008**, *58*, 481.
(8) Xiong, Z. T.; Yong, C. K.; Wu, G. T.; Chen, P.; Shaw, W.; Karkamkar, A.; Autrey, T.; Jones, M. O.; Johnson, S. R.; Edwards, P. P.; David, W. I. F. *Nat. Mater.* **2008**, *7*, 138.
(9) Yang, J. B.; Lamsal, J.; Cai, Q.; James, W. J.; Yelon, W. B. *Appl. Phys. Lett.* **2008**, *92*, 091916.
(10) Lin, Y.; Mao, W. L.; Mao, H. K. *Proc. Natl. Acad. Sci. U.S.A.* **2009**, *106*, 8113.
(11) Sakintuna, B.; Lamari-Darkrim, F.; Hirscher, M. *Int. J. Hydrogen Energy* **2007**, *32*, 1121.
(12) Wu, H. *ChemPhysChem* **2008**, *9*, 2157.
(13) Chen, P.; Xiong, Z. T.; Luo, J. Z.; Lin, J. Y.; Tan, K. L. *Nature* **2002**, *420*, 302.
(14) Janot, R. *Ann. Chim. Sci. Mater.* **2005**, *30*, 505.
(15) Ichikawa, T.; Leng, H. Y.; Isobe, S.; Hanada, N.; Fujii, H. *J. Power Sources* **2006**, *159*, 126.
(16) Xiong, Z. T.; Hu, J. J.; Wu, G. T.; Liu, Y. F.; Chen, P. *Catal. Today* **2007**, *120*, 287.
(17) Zalkin, A.; Templeton, D. H. *J. Phys. Chem.* **1956**, *60*, 821.
(18) Cunningham, P. T.; Maroni, V. A. *J. Chem. Phys.* **1972**, *57*, 1415.
(19) Murli, C.; Song, Y. *J. Phys. Chem. B* **2009**, *113*, 13509.
(20) Song, Y.; Murli, C.; Liu, Z. X. *J. Chem. Phys.* **2009**, *131*, 174506.
(21) Xie, S. T.; Song, Y.; Liu, Z. X. *Can. J. Chem.* **2009**, *87*, 1235.
(22) Liu, A.; Xie, S. T.; Dabiran-Zohoory, S.; Song, Y. *J. Phys. Chem. C* **2010**, *114*, 11635.
(23) Chellappa, R. S.; Chandra, D.; Somayazulu, M.; Gramsch, S. A.; Hemley, R. J. *J. Phys. Chem. B* **2007**, *111*, 10785.
(24) Mao, H. K.; Xu, J.; Bell, P. M. *J. Geophys. Res.* **1986**, *91*, 4673.
(25) Dong, Z. H.; Song, Y. *J. Phys. Chem. C* **2010**, *114*, 1782.
(26) Walrafen, G. E. *J. Chem. Phys.* **1964**, *40*, 3249.
(27) Walrafen, G. E. *J. Chem. Phys.* **1966**, *44*, 1546.
(28) Walrafen, G. E. *J. Chem. Phys.* **1967**, *47*, 114.
(29) Nibler, J. W.; Pimentel, G. C. *Spectrochim. Acta* **1965**, *21*, 877.
(30) Bohger, J. P. O.; Essmann, R. R.; Jacobs, H. *J. Mol. Struct.* **1995**, *348*, 325.
(31) Day, D. H.; Sinclair, R. N. *J. Chem. Phys.* **1971**, *55*, 2807.

JP107285R